PAPER

A shadowgraphy approach for the 3D Lagrangian description of bubbly flows

To cite this article: F Di Nunno *et al* 2020 *Meas. Sci. Technol.* **31** 105301

View the article online for updates and enhancements.

A shadowgraphy approach for the 3D Lagrangian description of bubbly flows

F Di Nunno[1] , F Alves Pereira[2] , F Granata[1], G de Marinis[1], F Di Felice[2], R Gargano[1] and M Miozzi[2]

[1] University of Cassino and Southern Lazio, Department of Civil and Mechanical Engineering (DICEM, Via Di Biasio, 43, 03043 Cassino, Frosinone, Italy
[2] National Research Council, Institute of Marine Engineering (CNR-INM), Via di Vallerano, 139, 00128 Rome, Italy

E-mail: massimo.miozzi@cnr.it

CrossMark

Abstract
A 3D volumetric technique for measuring the evolution over time of the kinematic and geometric characteristics of the bubble population in multiphase flows at moderate void fraction is here proposed. The method is based on a shadowgraphy approach and requires a set of calibrated and synchronized cameras, each placed in front of a bright screen. Synchronized, 2D images of the bubbly flow are analyzed to extract the outline of the bubbles as seen from every camera. Then, each bubble is separately identified as a 3D volume described by the intersection of the cones having vertices on the optical center of each camera and passing through the contour of the bubble. Details about the implementation of the procedure, including the further refinements of the first rough bubble identification and the optimization of the number and geometric arrangement of the points of view, are reported against the results obtained on a reference set of spheres of known dimensions. Application on isolated bubbles demonstrates the ability of the procedure to extract quantitative and self-consistent information over time. These results are consolidated by a hint at a plunging jet test case with a significant void fraction, showing potential for application to situations of practical interest.

Keywords: two-phase flow, bubbly flow, volumetric shadowgraphy, space carving, bubble tracking

(Some figures may appear in colour only in the online journal)

1. Introduction

An accurate analysis of the bubble geometric features, distribution and kinematic characteristics in a two phase air–water flow is essential to achieve a greater knowledge on the bubble dynamics in a wide range of technical and natural applications. An incomplete list should include the cavitation induced by the propellers of high-speed boats and submarines, the effect of drag variation in the hydrodynamics of ships, the fundamental role in chemical structures (reactors, adsorption towers, heat exchangers, etc) and the key action in the processes of heat and mass exchange between the oceans and the atmosphere, just to name a few of the possibilities.

Several experimental studies on bubbly flows of different types have been performed using intrusive resistivity probes, which measure the air concentration and bubble velocities based on the difference of electrical resistivity between air and water [1, 2]. A high sampling frequency is supported by the direct contact of the intrusive probe with the flow (about 20 kHz for a double-tip conductivity probe), and allows one to faithfully follow the flow behavior [3, 4]. On the other side, the drawbacks due to the intrusiveness of those probes involves a partial alteration of the motion of both liquid and gaseous phase. Moreover, their point-like measurement requires the use of decomposition techniques on the detected air–water signal for the characterization of the flow turbulence [5].

A first step to overcome the aforementioned limitations was made by the introduction of the planar particle image velocimetry (PIV) in experimental studies focused on the liquid phase, this optical measurement technique being able

to provide measurements of two or three components of the flow velocity field over a planar section and without disturbing the flow [6–8]. Despite the recent advances in the application of PIV techniques for the simultaneous and separated analysis of two-phase air–water flow by means of phase discrimination algorithms [9–11], a robust statistical analysis of fluid kinematics is only possible for low void fraction or no-entrainment regimes, because of the reduced visibility of the seeding particles as the void fraction increases. More specifically, in these conditions the seeding particles are occluded by the air bubbles moving between the investigated section and the optics of the PIV system [12]. This leads to a lack of knowledge about the air-bubble kinematic processes which dominates high-void-fraction bubbly flows and suggests that, for the analysis of such kind of flows characterized by high void fraction and/or strongly three-dimensional dynamics, the investigated region should be extended from a section to a volume. The simultaneous analysis of the two phases in air–water flows can be achieved by means of the combination of two techniques: PIV for the water flow field and shadowgraphy for the air bubbles measurement and tracking [13–15].

Shadowgraphy is a well-known flow visualization technique that highlights the difference of refractive index at the interface between a body and its surrounding medium. It is a simple technique that requires a light source and a recording plane on which to project the shadow of the different phases. The efficiency of the method is particularly high in the presence of large differences in refractive index, as it is between water and air [16].

The shadowgraphy technique has been used, in combination with image analysis algorithm, for air bubble tracking and measurement [13, 14, 17–19]. The application of these techniques involves the evaluation of the bubble geometric features based on the projection of the bubble boundaries on the image frame. This way, the measurement accuracy is closely related to the number of points of view and their geometrical relationships. The aforementioned studies adopt a single camera located in front of the investigated section. The single point of view provides only the shape and orientation of the air bubble in the plane orthogonal to its optical axis, thus the volume, the three-dimensional aspect ratio and orientation of the bubble cannot be directly observed and measured. A first improvement can be obtained by adopting two points of view having an orthogonal optical axis, but the resulting 3D intersection between the cones will be characterized by corners and edges that make the results far from acceptable. The shape and orientation of the air bubble obtained with two points of view require the use of refinement algorithms to better approximate the bubble geometry, e.g. bounding box method [20] and slicing method [21]. Yet, bubbles embedded in flows characterized by a high void fraction and/or strongly three-dimensional dynamics may have complex geometry that cannot be described using the aforementioned algorithms.

Here we report about the implementation of a 4-camera, 3D volumetric shadowgraphy technique and validate its accuracy against the benchmark measurement of buoyant, rigid spheres of known size, rising in still water. The detection of the size and shape of the spheres is made possible by a space carving algorithm [22]. Then, the same technique is applied to a set of isolated air bubbles having a different diameter, rising in still water, to investigate its capabilities in describing the bubble kinematics and deformations in time. The use of the shadowgraphy technique with relatively fast cameras allows us to follow the spatial-temporal evolution of individual air bubbles [23] and a tracking algorithm provides the 3D Lagrangian description of the bubble path. The tracking algorithm is based on the local form of the optical flow approach [24] and is used to find the bubbles correspondence in successive 2D images. This procedure allows a check about the mutual consistency of results both in space and frequency domains and with literature data. Finally, the shadowgraphy is applied to a set of test cases of a vertical plunging jet with several flow rates. The goal of this last application is to show the effectiveness of the proposed technique as a tool for the detailed analysis of air bubbles in two-phase air–water flows, also in the presence of relevant void fractions.

2. Experimental setup

This paper reports the main characteristics of the proposed shadowgraphy approach when applied to the description of the gaseous phase in a two-phase flow by grounding on three different *ad-hoc* designed experiments of increasing complexity. The focus moves from the benchmarking case of the rising of a rigid and buoyant sphere of known diameter to the capture of the population of bubbles trapped by a jet plunging on the free surface, passing through the characterization of a single, deformable rising bubble.

All the experiments share the same general arrangement, which consists of an octagonal base tank of side $L = 230$ mm and height $H = 500$ mm, made in transparent plexiglas to allow the optical access, an image acquisition system and a backlight illumination (figures 1 and 2).

The images acquisition system relies on two couples of Dalsa Falcon 1.4M100 cameras, whose CMOS sensor has a resolution of 1400×1024 pixels. The cameras mount 35 mm focal length lenses and are placed in front of two orthogonal tank sides, as shown in figure 1, with an azimuthal angle of $90°$ and an elevation angle of $\pm 15°$ from the horizontal plane (details in figure 3). Each couple of cameras is connected to Camera-Link frame grabbers (DALSA Coreco Imaging X64-CL): the whole acquisition chain allows a full-frame data stream of 100 frames per second (fps), which can be increased by reducing the frame size. As described below, the data stream is adapted to the characteristic time-scale of each experience, while the exposure time is kept constant and equal to 400 μs. The frame grabbers are hosted in the PCIx slots of an end-user PC, equipped with 64 GB of RAM and with a couple of solid state disks (SSD). An in-house acquisition software addresses the image streams from the frame grabbers to a circular buffer allocated in the RAM and eventually on SSD disks, with a First In First Out manipulation scheme. The system allows for the acquisition of synchronized image sequences whose length is limited only by the SSD disks capacity. The backlight illumination is provided by a couple
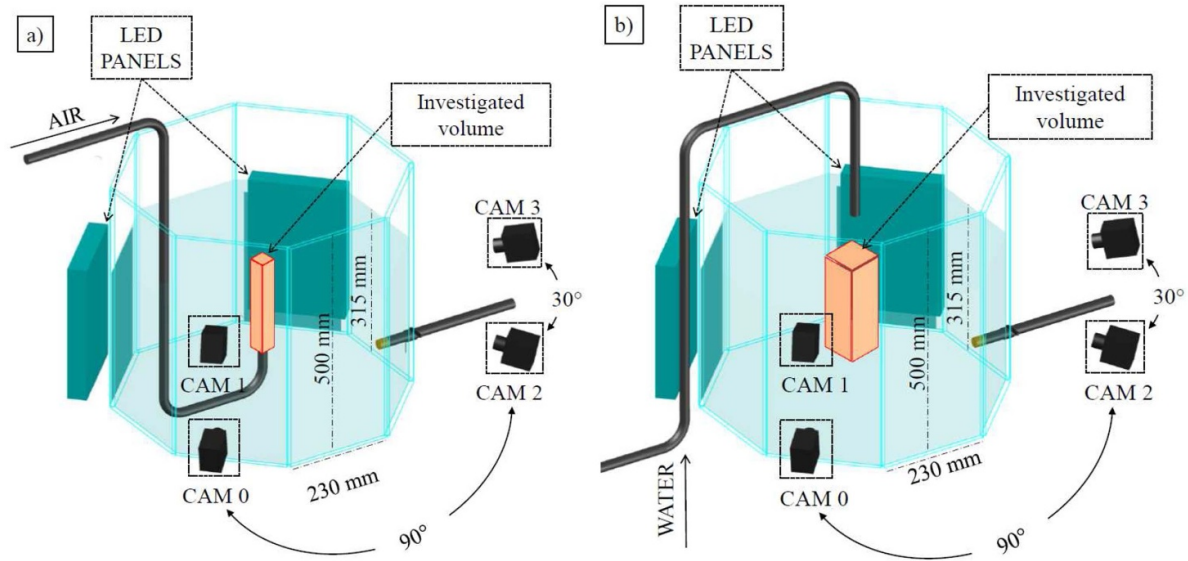
Figure 1. The basic experimental setup consists of a octagonal tank, two light panels and a set of four cameras. Different arrangements are reported for the rising sphere and bubble in still water (a) and the plunging jet (b). The clamping system for the rising sphere is not reported for the sake of readability. The investigated volume is the same for both the buoyant sphere and the rising bubble experiments.
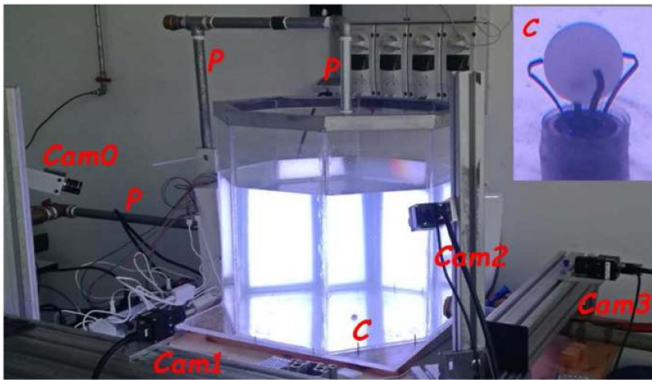

Figure 2. A photo of the experimental setup with the octagonal tank, the bright screens in the background and the cameras. The feeding tube of the plunging jet is labeled '*P*', while the clamping device for the release of the rigid balls, visible on the bottom of the tank, is labeled '*C*' and detailed in the insert at the top right.

of rectangular LED panels with a dimension of 297×210 mm and a power of 30 W. Panels are placed on the opposite sides of the tank with respect to the two couples of cameras (figure 2).

In addition to the general experimental arrangement, each of the three reported experiments has required the adoption of specific setup adjustments.

2.1. Rigid buoyant sphere

We checked the accuracy of the reconstruction algorithm by testing it on the rising of buoyant, rigid polypropylene spheres of known diameter $D_S = [7.94$ mm, 10 mm, 12.7 mm, 15mm$] \pm 0.05$ mm and density $\rho = 0.87$ g/cm^3 (RGPBALLS®). Spheres are released individually from the center of the bottom wall of the tank by means of a clamping

device (figure 2, top-right insert). Images of their rising are acquired by the acquisition system and analyzed by the shadowgraph algorithm as described in the following. The comparison of the estimated size with the known one provides a quantitative evidence of the measurement chain accuracy.

2.2. Isolated rising bubble

The second setup configuration is based on a steel pipe of three different diameters $D_P = [4.5$ mm, 7 mm, 9 mm$]$, which provide the release of isolated air bubbles. The axis of the steel pipe is placed along the center line of the tank and the nozzle is located at 140 mm from the bottom of the tank (figure 1(a)). The investigated volume for the cases of the rigid sphere and of the isolated bubbles extends from the nozzle to 126 mm upward (*x*-direction), and from -9 mm to 9 mm spanwise (*y*-direction) and depthwise (*z*-direction).

2.3. Plunging jet

The last and most complex configuration considers a water jet that falls from a downward oriented steel pipe, plunging onto the free surface (figure 2). The pipe is aligned to the center line of the tank and has a nozzle of diameter $D_J = 21$ mm, placed at a distance of $14D_J$ from the walls. The falling height is $H_J = 5D_J$, while the fluid depth is $15D_J$, kept constant with the outlet gate valve of the tank (figure 1(b)). The water flows in a closed circuit, moved by a centrifugal pump with a flow rate measured in time with an electromagnetic flowmeter.

The plunging jet experiment requires a larger investigated volume than the previous setups, which extends from the free surface to $6.5D_P$ streamwise (*x*-direction vertical), from $-2.5D_P$ to $2.5D_P$ spanwise (*y*-direction) and from $-1D_P$ to $1D_P$ depthwise (*z*-direction), while the LED panels illuminate the investigated volume from the impinging point to a depth

equal to $8D_P$ (figure 1(b)). It is to notice that the increase of the investigated volume along with the spanwise and depth-wise directions adopted for the plunging jet case has required the increment of the image size, this leading to a reduction of the frame rate from 275 Hz to 130 Hz.

3. Measurement principles

The basic principle of the volumetric shadowgraphy lies upon the evaluation of the three-dimensional position, shape and motion of the air bubbles, based on their boundaries or silhouettes observed from different points of view [23]. The projection of each boundary in the three-dimensional space defines a cone having as axis the straight line passing through the optical center of the digital camera lens and the bubble centroid. Figures 3 and 4 illustrates this principle. Here, the image plane (in gray) represents a projection plane $O_ix_iy_i$, $(i = 1,..,n$, where n is the number of cameras). It is identified by an origin O_i and a local coordinate system $x_iy_iz_i$, where the x- and y-axes are oriented as the sensor grid, the z-axis indicates the camera optical axis direction. The z-axis through the origin O falls on the center of the camera sensor (i.e. the center of the image). The four object silhouettes, observed by the four cameras, are projected from the respective image plane (in gray) to the space $O_wX_wY_wZ_w$, until they cross each other. The volume defined by the intersection of the conic projections embeds the observed object and greater precision can be achieved using a higher number of cameras, arranged in order to observe the object from different points of view.

The application of volumetric shadowgraphy requires an accurate photogrammetric calibration in order to evaluate the camera's intrinsic and extrinsic parameters [25]. Knowing the latter, it is possible to project in the 3D space the n cones, related to the n cameras, for each bubble inside the investigated volume. The intersection of the n cones defined by the bubble silhouettes provides its convex hull [22]. Furthermore, since the shape of the bubbles can be roughly considered as spherical or ellipsoidal, an ellipsoid fitting has been used to evaluate different bubble features, such as the principal semi-axes directions ($\vec{ax}_{0,1,2}$) and length ($ax_{0,1,2}$, where $ax_0 < ax_1 < ax_2$), eccentricity ($e = ax_0/ax_2$) and rotation angle [26].

3.1. Camera calibration

Camera calibration is aimed at evaluating the camera parameters, both extrinsic and intrinsic. Through these parameters it is possible to correct images from lens distortion and evaluate the camera sensor location with respect to the investigated volume and *vice-versa*, in order to project the images from their local 2D, discrete pixel reference system to continuous, 3D world units, thus allowing for a measure of the recorded objects ([25] among the others). The estimation of the camera parameters takes place through a well established calibration procedure [27] which involves the use of a specific target, where a *World* reference system $O_wX_wY_wZ_w$ is defined. In the present work, a planar chessboard 90×50 mm with squares of 5 mm $\pm$ 0.02 mm in side, stuck on a planar ($Z_w = 0$) steel plate was used.
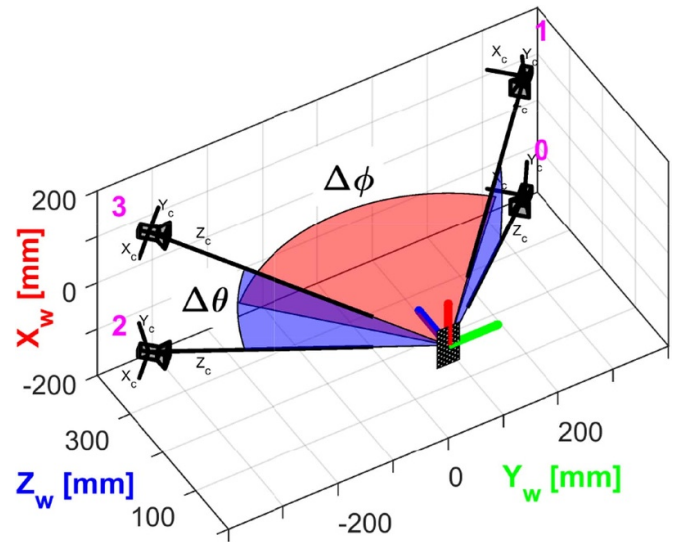

Figure 3. Camera Configuration A, $\Delta\phi = 90°$, $\Delta\theta = \pm 15°$. Azimutal $\Delta\phi$ and elevation $\Delta\theta$ angles refer to horizontal (red) and vertical (blue) planes respectively. A chessboard target allows for a space calibration.
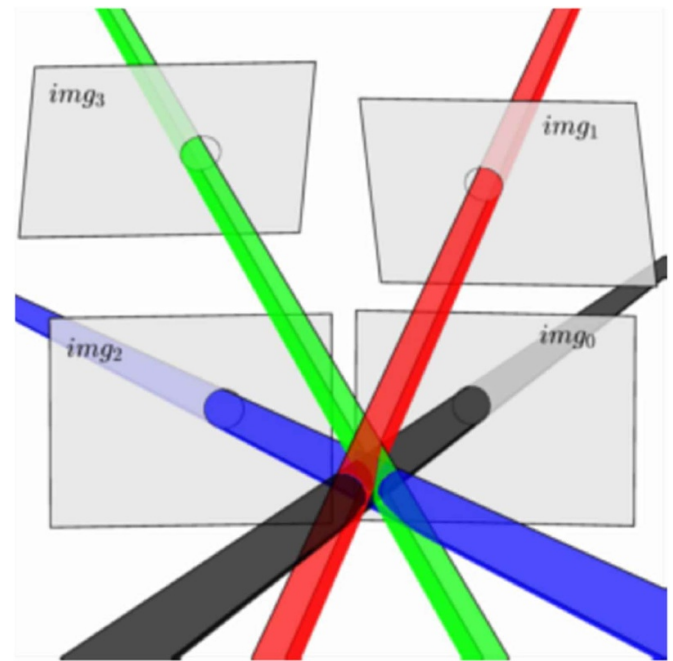

Figure 4. Measurement principle. The intersection of conic projections having apex in the cameras center of view and defined by the silhouette of the object on the plane of each image identifies a volume that embeds the object itself.

Simultaneous recording by all the cameras of 40 images containing the entire translated and rotated target provides the basis for the camera overall camera system calibration. The accurate corners identification in each target image allows one to finalize a preparatory and separated camera calibration procedure for each camera and then to move to a double stereo calibration for the couples of cameras, e.g. $Cam_0 - Cam_1$ and $Cam_2 - Cam_3$ [28, 29]. Having in hand the extrinsic

parameters of each camera referred to the same common target, we firstly evaluate the relative position and orientation of Cam_1 to Cam_0 and of Cam_3 to Cam_2 and subsequently we estimate the position and orientation of the two camera couples both relative and absolute, with respect to the world coordinate system. This last step provides the mapping of the target and, consequently, of the whole investigated volume.

With the aim to check the influence of the geometry of the camera system on the overall accuracy of the process and to move towards an optimum for the spatial arrangement of the points of view, two different configurations have been compared, namely Configuration A (figures 3) and Configuration B. In the former configuration, azimutal angles between optical axes of $Cam_1 - Cam_3$ and $Cam_0 - Cam_2$ are the same ($\Delta\phi = 90°$) so as the elevation angles between $Cam_0 - Cam_1$ and $Cam_2 - Cam_3$ ($\Delta\theta = \pm 15°$). On the contrary, in the latter configuration the azimutal angles between $Cam_1 - Cam_3$ and $Cam_0 - Cam_2$ are different ($\Delta\phi_{02} = 33.75°$, $\Delta\phi_{13} = 135°$) while the elevation angles are the same ($\Delta\theta_1 = 15°$, $\Delta\theta_2 = -15°$).

A first estimation of the accuracy of the camera calibration procedure, is given by looking at the reprojection errors, calculated as the distances, in pixels, between detected and reprojected corners. More specifically, the reprojection errors are calculated through the projection of the corner from the world coordinates, represented by the target checkerboard, to the image coordinates, by using the calibrated camera parameters. The results reported in figure 5 and in table 1 show better performances of Configuration A for all the four cameras (black crosses), being their values in the range between -1.5 pixel to 1.5 pixel (corresponding to -0.2 mm to 0.2 mm). On the contrary, the reprojection errors in Configuration B ranges between -3 pixel to 3 pixel, with higher values for Cam_1 and Cam_3 because of their wider angle to the optical center with respect to Cam_0 and Cam_2. Therefore, under the evidence of lower reprojection errors confirmed in repeated applications of the proposed calibration procedure, the spatial arrangement of the points of view in Configuration A is adopted for the experimental activity reported below. It is to notice that the wider reprojection error can be associated to the planar nature of the adopted target, because all the cameras have to see it simultaneously during the calibration procedure and large angles of view can amplify the uncertainties. The adoption of a 3D target may reduce such kind of association and its test is planned for future activities.

3.2. Space carving

The space carving technique provides the convex hull of the reconstructed object starting from the projection of the object silhouettes observed from different views. The procedure consists of the following steps:

(a) projection in the Euclidean space of the four cones, defined as the set of half-lines connecting the cameras center of view, e.g. the cones apex, to all of the points on the four
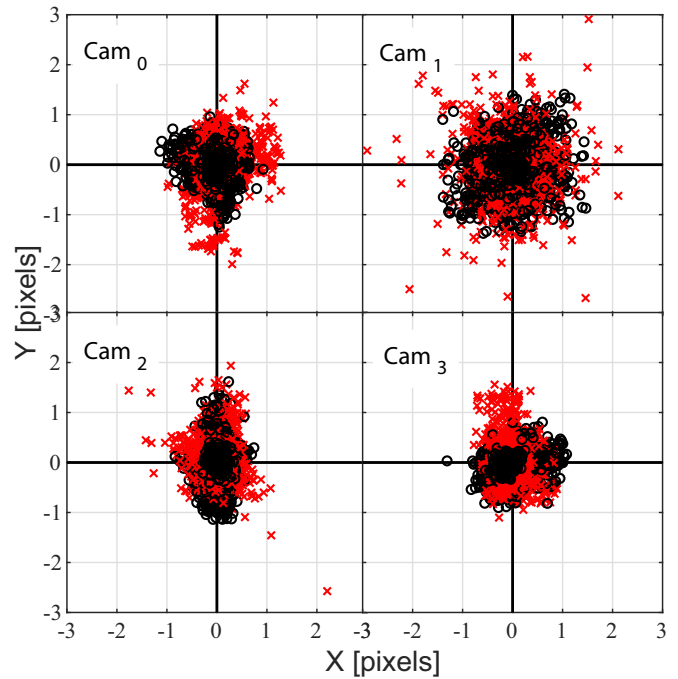

Figure 5. Reprojection errors for Configuration A (black circle) and Configuration B (red cross). Reprojecton errors refer to the final mapping of the four cameras and exhibit lower magnitudes in Configuration A.

contours of the object silhouette captured by the different points of view (figure 3 and figure 4);

(b) computation of the four Delaunay triangulations, one for each cone;

(c) definition of a three dimensional mesh to evaluate the volume of intersection of the four cones (one for each investigated bubble). The center of the mesh corresponds to the object centroid, the voxel side is of 0.10 mm, small enough to allow an accurate reconstruction of the objects investigated in the present work and side assessed through a series of measurements aimed at providing the maximum size of the air bubbles, which led to a mesh side of 16 mm for the plunging jet test;

(d) internal common points research between the Delaunay triangulations. From this operation a mask that contains zeroes (external points) and ones (internal points) is obtained; and

(e) the three-dimensional triangulation of the voxels centroids belonging to the isosurface from the mask data provides the rough boundary of the observed object.

Figure 6 shows an example of how the space carving technique works in the reconstruction of a sphere with four cameras. Figure 6(a) reports a real sketch of the influence of the number of points of view and of their position on the accuracy of the final result. The elements measured on the original 2D images, i.e. the bubble contours extracted from the four cameras, are reported as black, crimson, green and brown closed curves that represent the tangent *loci* between the cone of view
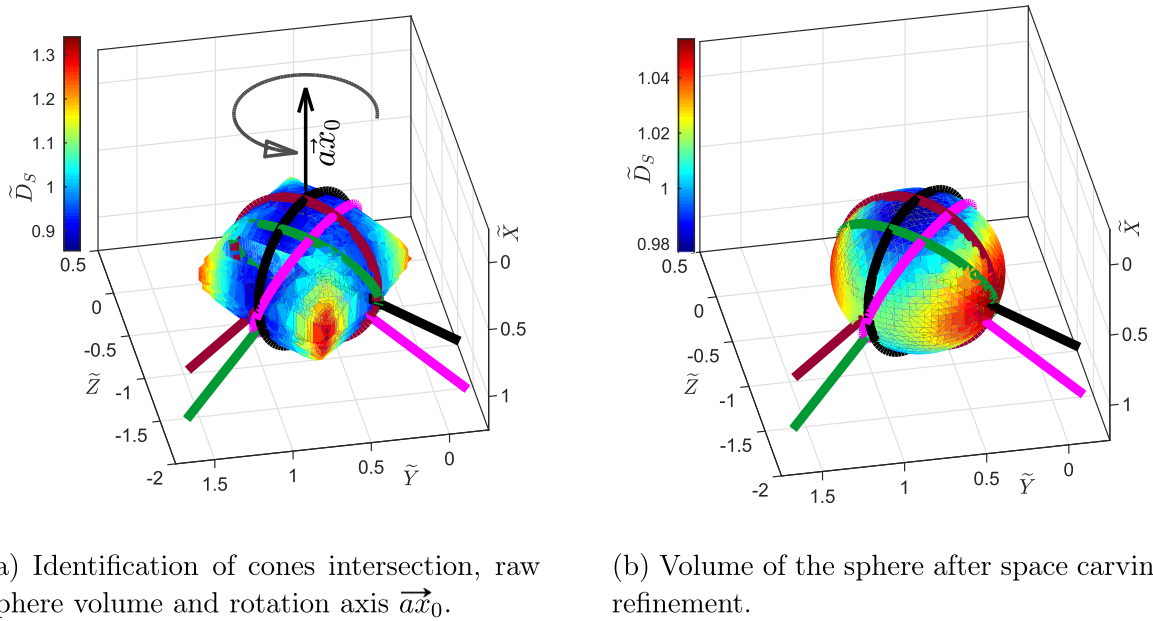
(a) Identification of cones intersection, raw sphere volume and rotation axis $\vec{ax}_0$.

(b) Volume of the sphere after space carving refinement.

Figure 6. Errors colormap referring to the ratio between estimated and true sphere diameter. Tangent *loci* between cones and sphere are reported as black, crimson, green and brown closed curve while cones axes are shown as lines departing from the closed curves center to the points of view. Sphere diameter D_{S2}.

and the sphere. A set of four lines with the same colors connect the geometric center of each best fitting ellipse to the camera optical center; they represent the axis of the cone of view. When the operation of cone intersection takes place, the resulting object is strongly affected by the lack of a point of view orthogonal to the Y–Z plane: solid cones intersection generates strong sphere distortions at intermediate positions. The error distribution (departure from $\widetilde{D}_S = 1$) reported in figure 6(a) quantitatively confirms a good approximation of the sphere along the tangent curve. On the contrary, at intermediate positions where the cones intersect themselves, the discrepancy between the sphere estimation and the real one rises up to 30%. The rough level of accuracy imposes a refinement of the volume shape, as described in the following.

3.2.1. Space carving refinement. An optimal solution to catch the true object's shape would be the insertion of a point of view orthogonal to the plane $X = 0$, however this was not possible because of the setup design and because of the presence of the free surface. A procedure is then applied to refine the rough sphere contour, which consists of a rotation of the previous space carving operation by half of the cameras azimutal distance $\Delta\phi/2 = 45°$. In the analysis of the rigid spheres, rotation occurs around an axis orthogonal to the plane $X = 0$ (plane of θ-symmetry of the video cameras' location), passing through the center of the equivalent ellipsoid (see figure 6(a)). It is applied to the whole set of 3D points, previously identified with cones intersection, by following the classical rigid body rotation approach (see [30] among the others).

After the computation of the Delaunay triangulations for both rotated and non-rotated objects, the refinement ends following the steps (iv) and (v) reported in section 3.2, with the internal common point research between the two Delaunay

triangulations of the rotated and non-rotated sets of points. The final result is reported in figure 6(b). Errors in proximity of the closed curves of tangency between the sphere and the projected cones remain almost the same, while the deformations in the intermediate locations are drastically reduced, providing an overall accuracy of the sphere's radius between -2% to 4%.

It is worth noting that the space carving procedure smooths the regions close to the intersection of the surfaces of the cones, by a surface of revolution generated after the rotation of the curve where the cones are tangent to the object (black, crimson, green and brown curves in figures 6(a) and (b)), implicitly assuming the hypothesis of axial symmetry. This approach has physical soundness when dealing with isolated rising bubbles, where an equatorial plane can be identified in the equivalent (oblate) ellipsoid, as will be introduced in section 4.2.1. In that case, the rotation occurs around an axis ($\vec{ax}_0$) passing through the ellipsoid center and orthogonal to the equatorial plane. However, it must be acknowledged that the overall approach is only valid for convex objects and that inner concavities cannot be retrieved. Further refinements to take into account more complex object shapes are planned for future works.

3.3. Rigid sphere and air bubble detection and tracking

In shadowgraphy images of a bubbly flow, light from the background bright screen meets air–water interfaces from one or more bubbles and scatters both by total reflection and refraction followed by internal reflections and refractions [31], such that the light intensity collected on the camera sensor varies accordingly. In particular, the strongest attenuation occurs at the bubble edge. On this basis, we assume the ansatz that
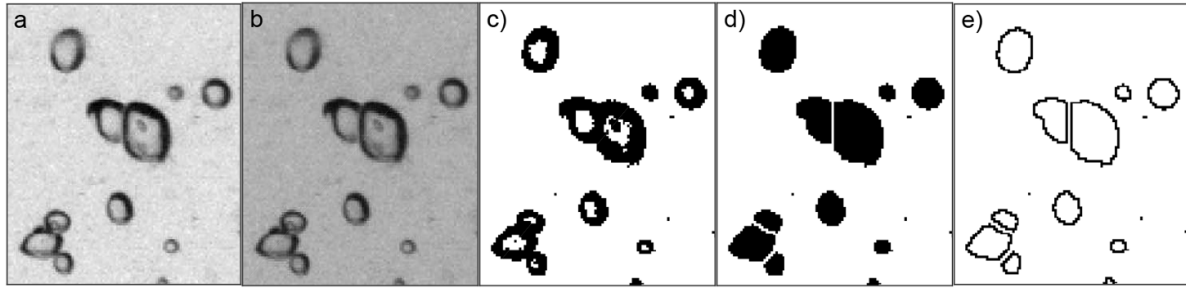
Figure 7. Bubble contour identification. (a) Original image. (b) Background removal. (c) Thresholding. (d) Watershed. (e) Outline and final contour.

the image intensity of pixels excited by light rays close to the edges of bubbles is lower than the background. In the first step, the bubbles and their boundaries are detected by applying the procedure schematically reported in figure 7.

For each camera, the image background is calculated as the median over the entire sequence and subtracted to every image (figure 7(a) to (b)). This step minimizes the reflections from fixed objects and light non-uniformity within resulting images, thus emphasizing the contribution of moving objects like the bubbles (figure 7(b)).

The second step concerns the binarization of the images (figure 7(c)), which transforms the intensity value of each pixel with intensity above a given threshold to a maximum (i.e. 1) while each pixel whose intensity is below a given threshold is reduced to a minimum (i.e. 0). The optimal threshold is given by the *IsoData* algorithm [32]. Here the optimal threshold is automatically chosen as a result of an iterative process able to detect the entire bubble boundary also when bubbles coalesce in complex clusters, as shown in figure 7(c).

The difficulty in managing the bubbles overlap inside bubble clusters is overcome by the application of a watershed technique [9, 33]. This technique assumes a gray-scale digital image like a relief map, with the gray levels of pixels indicating their elevation in the relief. Considering a bubble cluster as a series of hydrographic basins adjacent to each other, the watershed lines allow their division and, consequently, their detection, see figure 7(d).

The last step in bubble boundary identification consists in the detection of their boundaries $B_i(x, y)$, $i = 1, ..., N_t$, where B is a discrete vector of contours and N_t is the number of contours identified within the image at time t. Notwithstanding the relatively common use of techniques with sub-pixel accuracy, here the bubble boundary has been extracted by considering the pixel outline of the internally connected regions considered as isolated bubbles (figure 7(e)). The recorded shadowgraphy images of bubbles exhibit a thick dark boundary at the air–water interface, induced by the change in the refractive index due to the surface curvature variation, which masks the subpixel details (figure 7(b)). Moreover, the overall geometric arrangement deals with a high spatial resolution (≈ 0.1 mm/px) and a subpixel refinement will fall below this threshold. The voxel side adopted for the discretization of the 3D volume is again 0.1 mm, so the subpixel adjustment at image level could fall inside the same voxel obtained with a

pixel-level boundary estimation. Grounding on these observations and considering that the sub-pixel location estimation is a time-consuming analysis, its cost-benefits ratio appears to be disadvantageous for the present application.

The application of the bubble identification procedure provides a set of bubble boundaries for each image, in each of the sequences provided by the cameras, i.e. $\mathfrak{B}_{2D}^c(t) = B_i(x, y)$, where c is the camera identifier. The correspondence between boundaries of the same bubble at different times (i.e. in different images) is extracted on the basis of the results of the Lucas–Kanade algorithm [24] applied to 2D image sequences of bubble boundaries. The bubble boundary correspondence allows one to track them in time. The shadowgraphy applied to the set of $\mathfrak{B}_{2D}^c(t)$ provides the 3D position of the bubble sets at each time t, namely $\mathfrak{B}_{3D}(t)$. On the basis of the knowledge of the Lagrangian behavior of the bubbles, a 3D description of the bubble evolution is obtained.

4. Results and discussion

In what follows, if not otherwise specified, lengths are normalized as $\widetilde{X} = X/D$, where D is the characteristic diameter of the configuration under consideration. It can be one of the four D_S diameters of the rigid sphere case, one of the three D_P pipe diameters in the isolated bubble case or the nozzle dimension D_J in the plunging jet application. Accuracy of the estimated diameter D_{est} in the benchmark tests is expressed as $\widetilde{D} = D_{est}/D$, where D is one of the aforementioned design diameters. Normalization of other quantities is done against their maximum value and is explicitly specified in the text.

4.1. Technique validation

The test of the reconstruction algorithm on buoyant polypropylene spheres of known size provides a quantitative estimation of the accuracy of the procedure in the calculus of the equivalent sphere radius. Our validation test is limited to a spherical object as this trivial geometry is the baseline shape of the bubble topology under study in this work. In this respect, the test provides the fundamentals for future validation on shapes of higher complexity that could find interest in a broader range of applications.

A single sphere is clamped on the bottom of the tank and then released (top-right inset of figure 2). During the sphere
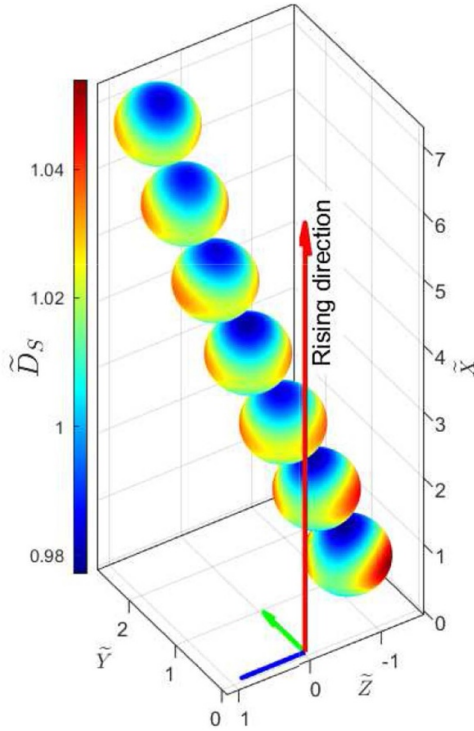
Figure 8. Time sequence of a sphere (D_{S_2}) position and accuracy of its volume estimation. The lower object corresponds to the object in figures 6.

Figure 9. $\widetilde{D}_S$ vs. $\widetilde{X}$ rising location. Dashed lines mark $\langle\widetilde{D}_S\rangle$ for each diameter: D_{S_1} ($\triangle$), D_{S_2} ($\square$), D_{S_3} ($\bigcirc$), D_{S_4} ($\diamondsuit$). X normalized by its extent.

ascent, driven by the buoyancy force, its size and motion can be measured. Figure 8 shows the sequence of positions occupied by the sphere with $D_{S_2} = 10$ mm during its rise inside the investigated volume, together with the estimated sphere diameter $\widetilde{D}$. The lower object of the sequence corresponds to the object in figures 6 and exhibits the higher discrepancies between $\widetilde{D}$ and its ideal value of 1. Larger under- and over estimations occur close to the intersections of the *loci* of tangency between the sphere and the projected cones but, on the contrary to what can be argued from figure 6(a), here the relationship with the cone intersection geometry is tainted by the further complexity introduced by the space carving refinement procedure, which requires an estimation of the equivalent ellipsoid to identify the center and the axis of rotation. However, the local distribution of $\widetilde{D}$ appears to be unchanged with the bubble rising. The four different spheres show values of $\langle\widetilde{D}\rangle$ in the range between 0.999 to 1.011, with a standard deviation $\sigma(D)$ between 0.001 2 mm, for the sphere with diameter 10 mm, to 0.003 8 mm, for the sphere with diameter 7.94 mm (figure 9). The time averaged value of $\widetilde{D}$ along the rising direction $\widetilde{X}$, $\langle\widetilde{D}\rangle$, is reported in figure 10(a) for results obtained by from different combinations of cameras.

A sketch of the results about the reconstruction algorithm accuracy is reported in table 1, in terms of the normalized diameters $\langle\widetilde{D}\rangle$. The estimation of the fitted ellipsoid provides the three principal semi-axes and their eccentricity e, expressed as the ratio between the time averaged value of the minor ($\langle\widetilde{D}_{\min}\rangle$) and major ($\langle\widetilde{D}_{\max}\rangle$) axis, ranges between 0.932 and 0.945.

Furthermore, a comparison between the results about the reconstructed sphere with diameter $D_{S_2} = 10$ mm obtained
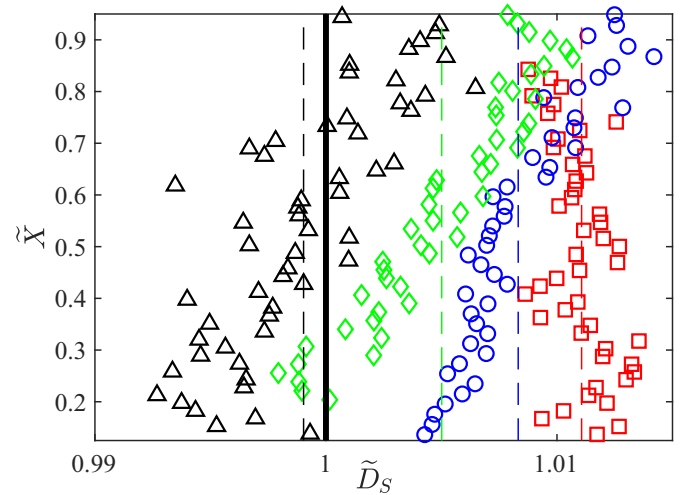
considering different camera groups is shown in figure 10(b). By moving from two to four cameras it can be noticed that the size of the reconstructed sphere gets closer to its true value, due to an increase of the number of intersected cones (figure 10(b)), It decreases from a value of $\langle\widetilde{D}\rangle$ equal to 1.034 for the couples *Cam1–Cam3* to 1.011 for the four cameras configuration. In order to better verify the accuracy of the reconstruction technique, the variation of the size measurement along the frame sequence has been also evaluated considering the normalized standard deviation $\Theta(\widetilde{D})$ (error bars in figure 10(a)), calculated as

$$\Theta(\widetilde{D}) = \sigma(\widetilde{D})/\langle\widetilde{D}\rangle \qquad (1)$$

where $\langle\widetilde{D}\rangle$ and $\sigma(\widetilde{D})$ are the mean and the standard deviation of the normalized diameters computed along the rising direction $\widetilde{X}$. As the number of cameras increases, a reduction of the coefficient of variation Θ is observed, with the minimum values measured for the four cameras configuration (see figure 10(a)). Therefore, we argue that the reconstruction technique with four cameras configuration is able to provide reliable results with limited errors on the estimation of the size and shape of the measured elements and that configurations with higher number of cameras may be able to further improve the reconstruction accuracy.

4.2. Rising bubble in still water

A 3D Lagrangian tracking algorithm has been applied to the volumetric data obtained with the shadowgraphy technique implemented here, providing the time-resolved size and location of each air bubble and consequently the velocity along their path [34, 35]. The technique has been initially applied to the detection of single bubbles. These bubbles are released individually from the bottom of the observation tank, by means of a steel pipe of three different diameters $D_P = [4.5$ mm, 7 mm, 9 mm]. Results are expressed normalized by their maximum value, e.g. $\widetilde{\Psi} = \Psi/\Psi_{\max}$ for volumes. Every bubble
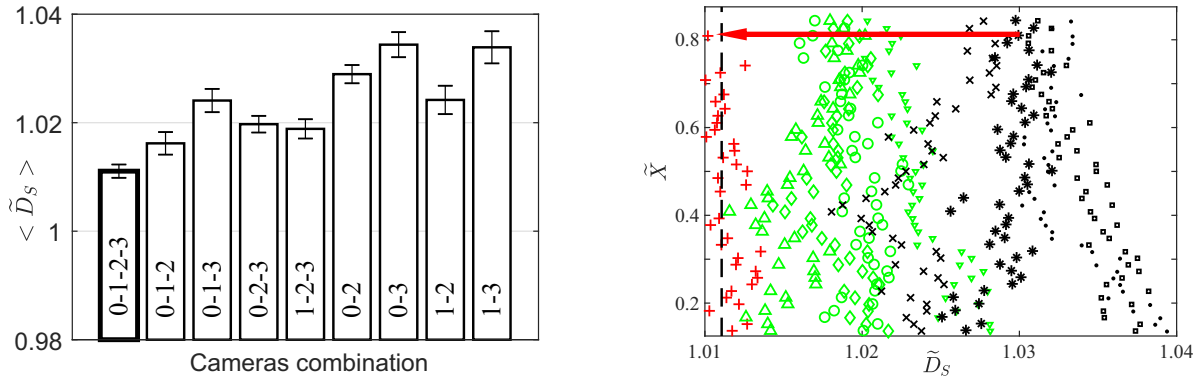
Figure 10. Aggregated and disaggregated accuracy in sphere diameter D_{S_2} estimation.

Table 1. Statistical parameters for the reconstruction algorithm accuracy. D_{true}: certified diameter of the sphere. $\langle D \rangle$: averaged diameter along the sphere's trajectory. $\sigma(D)$: diameter standard deviation along the sphere's trajectory. D_{min}, D_{max}: extrema of the sphere's radius along the sphere's trajectory. e: eccentricity. Errors are given as D_{est}/D_{true}.

Test case	D_{true} (mm)	$\langle D \rangle$		$\sigma(D)$ (mm)	D_{min}		D_{max}		e
		(mm)	Error		(mm)	Error	(mm)	Error	
1	7.940	7.932	0.999	0.007 6	7.670	0.966	8.178	1.030	0.937
2	10.000	10.110	1.011	0.002 4	9.830	0.983	10.4	1.040	0.945
3	12.700	12.806	1.008	0.005 2	12.254	0.965	13.208	1.040	0.932
4	15.000	15.074	1.005	0.007 0	14.52	0.968	15.434	1.029	0.941

can be represented by its equivalent ellipsoid, characterized by its center $C_{0e} = X_{0e}, Y_{0e}, Z_{0e}$, its axis direction $\vec{ax}_i$ and length ax_i, $(i = 0, 1, 2)$.

Unlike the polypropylene spheres considered, air bubbles are deformable objects that can change their shape and size during their rise, hence a case of interest to demonstrate the ability of the implemented technique in the reconstruction of objects characterized by complex geometries. Therefore, in order to evaluate the gradual shape and motion variations of the air bubbles, the image sequences are recorded at a frame rate equal to 275 Hz. This allows a correct time-resolved reconstruction of the air bubbles with an optimal pixel displacement of the bubble boundaries. Figure 11 shows the recorded and reconstructed sequence of positions taken by the air bubble, plotting one out of every five, for a clear and easy-to-understand representation, avoiding the overlap between bubbles on different frames owing to the high frame rate. The tracking of the individual bubble in terms of rigid translation of the bubble centroid, shifted away from the bubble centroid for the sake of clarity, is also reported. Furthermore, the dimensionless air bubble volume $\widetilde{\Psi}$ is represented. Although the air bubble injection mechanism has been designed to produce a gradual release of identical volumes of air, marked variations in bubble shape are observed near the outlet section, due to the bubble detachment from the nozzle. Subsequently, an air bubble expansion is observed: the bubble volume reaches maximum values at a vertical distance from the bottom of the tank close to $8D_P$, where D_P is the steel pipe diameter.

4.2.1. Shape and path oscillations.
The kinematics and geometric characteristics of the bubble at the three investigated

pipe diameters are compared in figure 12, where the evolution in time of the dimensionless volume $\widetilde{\Psi}$ (dashed line) and streamwise velocity $\widetilde{U}$ (continuous line) are reported along the whole bubble rising sequence. It can be noticed the onset of a phase opposition relationship in the first times for lower diameters D_{P_1} and D_{P_2}, while at higher diameter D_{P_3} the rising velocity increases its oscillation frequency and this relationship, although certainly present, is harder to identify. Moreover, the time evolution of the axes $ax_{0,1,2}$ (red, green and black line) of the equivalent ellipsoid is reported in figure 13, together with the bubble eccentricity (gray line) as the ratio between the minor axis ax_0 and the major axis ax_2 (rightside axis). The air bubble shape appears more spherical near the outlet section, while it shows a more elliptical shape during its rising with fluctuating values of the eccentricity e. Interestingly, the shape oscillation is in agreement with the streamwise velocity, with a more or less flattened shape as the streamwise velocity increases or decreases respectively. The same agreement can be observed between the axes of the equivalent ellipsoid (figure 13). Their behavior unveils the existence of an equatorial, almost circular section (plane $\vec{ax}_1(t) - \vec{ax}_2(t)$), where $ax_1(t) \approx ax_2(t)$, which oscillates in opposition of phase with the length $ax_0(t)$ along the orthogonal axis $\vec{ax}_0(t)$. This latter identifies the instantaneous axis of rotation adopted for the space-carving procedure.

The comparison between bubbles having increasing diameters shows a more spherical appearance, with smaller variations of shape and size, for the air bubble generated by the steel pipe with the smaller diameter (D_{P_1}), compared to D_{P_2} and D_{P_3}. These results are consistent with the physical properties of a bubble rising in still water. In particular, if the bubble is large enough, the action exerted by the water on
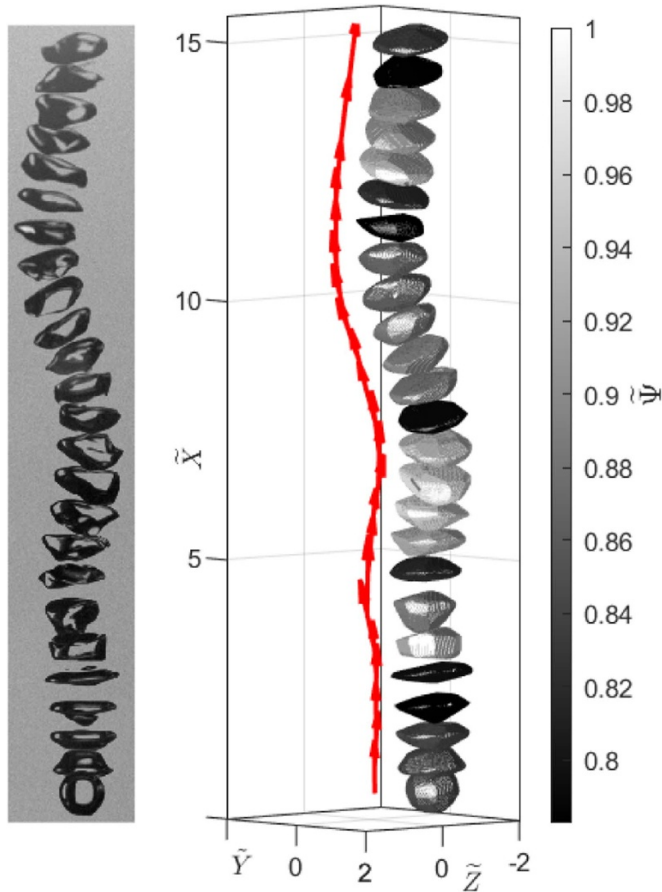
Figure 11. Rising bubble at $D_{P_2} = 7$ mm. Left: Sequence in time of images of one isolated bubble from one of the four points of view (Cam_0). Right: Sequence of reconstructed bubble positions along the rising direction $\widetilde{X}$. Gray tones report the normalized bubble volume $\widetilde{\Psi}$. Red arrows report the bubble trajectory and velocity along the whole sequence (slightly shifted for the sake of readability).

Figure 12. Time evolution of the isolated bubble rising velocity $\widetilde{U}$ (continuous line) and of the bubble volume $\widetilde{\Psi}$ for diameters D_{P_1} (top), D_{P_2} (bottom) and D_{P_3} (bottom). A phase opposition relationship between $\widetilde{U}$ and $\widetilde{\Phi}$ is noticeable in the first times for D_{P_1} and D_{P_2}.

the bubble surface overcomes the surface tension, involving a distorted oblate spheroidal shape. This effect is expressed through the Weber number $We = \rho U^2 * D_p / \sigma$, where U is the bubble velocity and σ is the surface tension. Large deformations occur for $We >> 1$. Here we have $1.76 < We_{D_{p_2}} < 10.20$ and $3.42 < We_{D_{p_3}} < 15.43$, respectively for D_{p_2} and D_{p_3}. For smaller bubble, like D_{P_1}, the water forces do not exceed the surface tension, with the latter that involves a spherical shape minimizing the air bubble surface area ($1.52 < We_{D_{P_1}} < 3.76$, [20]). A further support to the consistence of the reported results is provided by the phase plot in the Galilei–Eötvös plane $Ga-Eo$ (figure 1 in [36]), which subdivide the $Ga-Eo$ space in five distinct bubbles regimes with sharply defined boundaries. By defining the adimensional Galilei number as $Ga = \rho_w \sqrt{gR_{eq}} R_{eq} / \mu_w$ and the Eötvös number as $Eo = \rho_w g R_{eq}^2 / \sigma_w$ (where ρ_w is the water density, g is the gravity acceleration, R_{eq} is the bubble equivalent radius, μ_w is the water dynamic viscosity and σ_w is the water surface tension), the bubbles presented in this work have the coordinates $Eo = [0.76, 2, 2.9]$ and $Ga = [360, 750, 990]$. The line defining their location in the $Ga-Eo$ plane goes through the boundary between region *III* (case D_{P_1}), where the bubbles exhibit an oscillatory motion
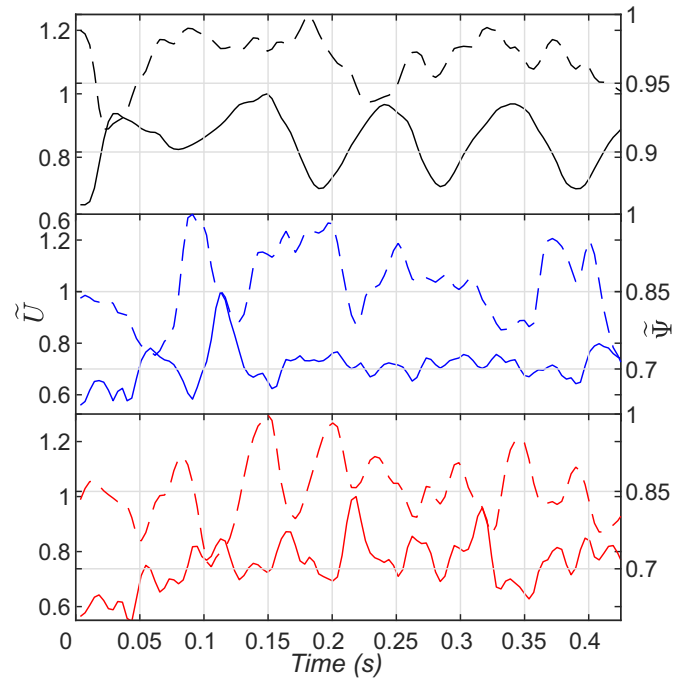
(zig-zag or spiral one), and region *IV* (case D_{P_2} and D_{P_3}), where a transition towards a peripheral breakup takes place. This transition occurs simultaneously with a change in bubble shape, i.e. from the oblate spheroid to the spherical cup with open, unsteady wake, as conceivable from eccentricity results in figure 13 and obtained following the classical $Eo-Re$ space classification of figure 8 in [37], where the Eo characteristic length is D_{eq}.

Further details about the relationship between the bubble shape, its velocity and its path oscillation are provided by the frequency spectra of the time history of the eccentricity, shown in figure 14. These spectra are obtained by applying the classical Fourier analysis to the time signal of e. With the aim to reduce the finite-length noise-related effects and to artificially increase the spectra resolution, the signal is convolved by a Hanning-like window and symmetrically zero-padded from 128 to 256 samples. The PSD sketched in figure 14 shows that the eccentricity oscillation frequency behaves in very peculiar ways at different bubble sizes, with the distribution of *PSD* occurring at fundamental frequencies and at their linear combinations. At smaller diameter D_P, the *PSD* of e exhibits a single, well defined peak at $f_{D_{P_1}} = 9.8$ Hz (black line and text). At intermediate diameter, two fundamental peaks are evident, one at $f_{D_{P_2}}^m = 7.52$ Hz and the other at $f_{D_{P_2}}^M = 10.74$ Hz, together with their linear combinations at $\sum f_{D_{P_2}} = 18.26$ Hz and at $\Delta f_{D_{P_2}} = 3.22$ Hz (blue line and text); at larger diameters, the fundamental peaks occur at $f_{D_{P_3}}^m = 7.52$ Hz and $f_{D_{P_3}}^M = 11.82$ Hz, together with their sum at $\sum f_{D_{P_3}} = 19.34$ Hz (red line and text).
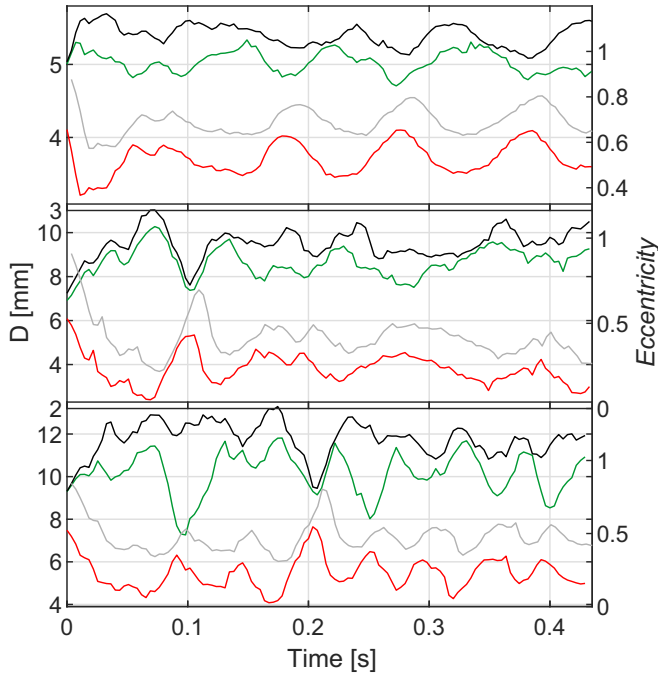
Figure 13. Axis of the equivalent ellipsoid ax_0 (red), ax_1 (green), ax_2 (black), together with eccentricity (gray) for D_{P_1} (top), D_{P_2} (middle) and D_{P_3} (bottom). The almost regular oscillations at D_{P_1} evolves towards more irregular changes at D_{P_2} and eventually doubles their frequency at D_{P_3} (see figure 14).
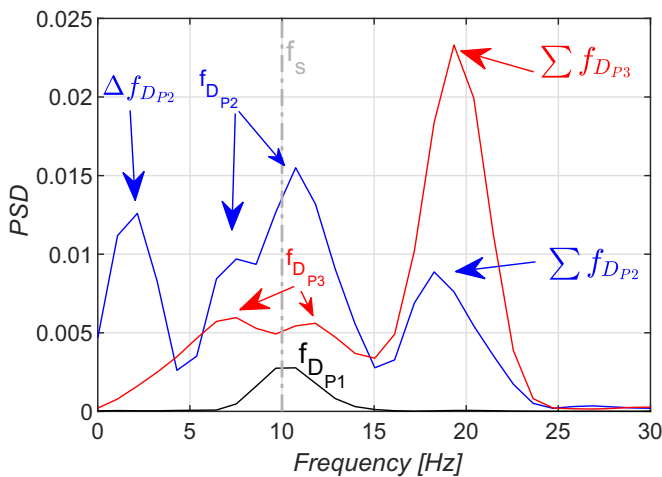

Figure 14. Frequency spectra of ecccentricity variation at increasing pipe diameters D_{P_1} (black), D_{P_2} (blue) and D_{P_3} (red) and shedding frequency of the bubble wake $f_s \approx 10$ Hz (gray, dash-dot line). Frequency peak at D_{P_1} is locked at f_s, while at D_{P_2} and D_{P_3} the fundamental peaks fall around f_s.

This complex and counterintuitive behavior can be associated again with the change in shape characters due to the passage between region *III* and region *IV* of the *Ga−Eo* diagram described beforehand and, more specifically, to the stability of the wake that develops behind the rising bubble. An insight about the wake stability is provided by the projection onto the *Y–Z* plane of the bubbles' path (figure 15). There, it can be observed the passage from a zig-zag trajectory for
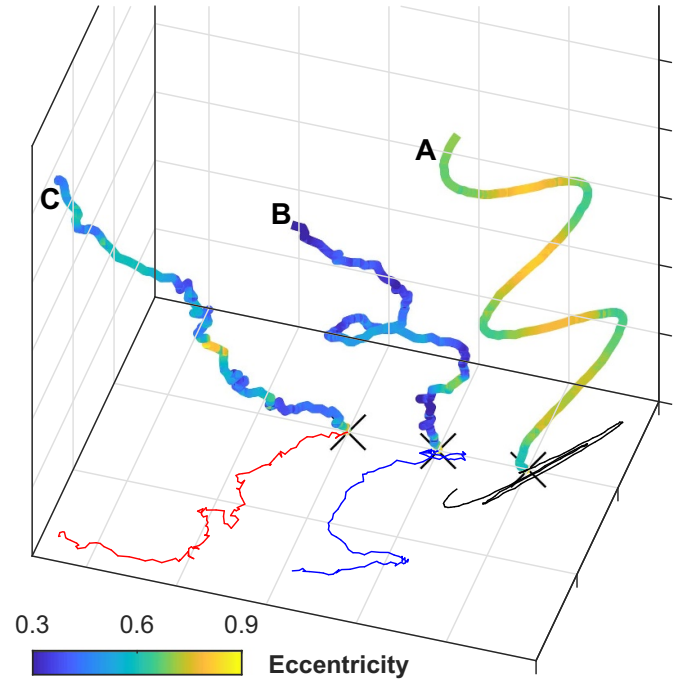

Figure 15. 3D representation of bubbles trajectory, colored by the eccentricity $e(t)$ and shifted for clarity along $\widetilde{Y}$. Their projection on the $\widetilde{YZ}$ plane is reported as well (black, blue and red curves for A, B and C trajectories). The bubbles' path evolve from a smooth zig-zag (D_{P_1}, A) to a more jagged spiral (D_{P_2}, B and D_{P_3}, C). Higher curvatures traits in zig-zag regime (A) correspond to more squeezed bubble shape, straight intervals to more spherical bubble appearance.

D_{P_1} (line A) to a spiral-like one for $D_{P_{2,3}}$ (lines B and C). Colors in 3D paths correspond to eccentricity values, while black, blue and red colors of 2D curves identify $D_{P_{1,2,3}}$ respectively. As reported by [38], the zig-zag condition is characterized by the presence of two equal-strength vortex pairs, which shed twice during a period of the pure zig-zag path. The zig-zag motion is triggered by the amounts of streamwise vorticities accumulated on the bubble interface, when a critical value is reached. However, when the balance between the counter-rotating vortices is broken, an angular velocity is induced between the asymmetric vortex pairs, driving the bubble to rise in a spiral path. Fourier analysis of the bubble path identifies a zig-zag frequency of $f_z \approx 5$ Hz for both D_{P_1} and D_{P_2}. On the contrary, no neat path oscillation frequency can be found at D_{P_3}. On these basis, it can be argued that the shedding of the wake locks the bubble oscillation [39] at the shedding frequency $f_s = 2 \times f_z \approx 10$ Hz (dash-dot, gray line in figure 14) and concentrates the spectral energy around f_s for D_{P_1}. Changes in the bubble shape modifies the balance of the rear vortexes; this induces a transition from zig-zag to spiraling of the bubble's path at D_{P_2} and D_{P_3} and excites modes at frequencies slightly lower and higher than f_s. Interestingly, under the zig-zag condition the intervals of the trajectory with a higher curvature are nicely associated with a low bubble eccentricity (oblate spheroid), while during the straightest sections the bubble takes on a more spherical appearance (figure 15, trajectory A).
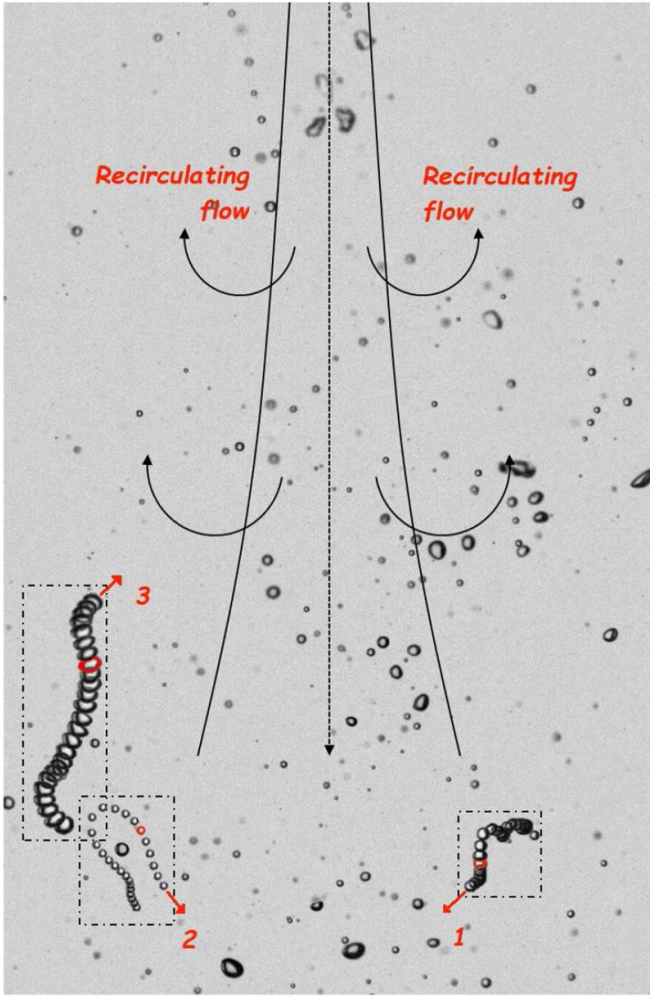
Figure 16. Snapshot of the bubble field at frame $fr = 8$ by Cam_1. Superimposition of 26 raw images from $fr = 0$ to $fr = 25$ for three trajectories (1, 2, 3). Red arrow in the bubble's displacement direction. Bubbles circled in red match the frame $fr = 8$.

A comparison of present results to what is found in literature can be done following [39], where two modes of ellipsoidal harmonics, namely modes $(2,0)$ and $(2,2)$, are considered:

$$f_{2,0} = \frac{1}{2\pi} \sqrt{\frac{16\sqrt{2}e^2\sigma_w}{\rho_w(e^2+1)^{3/2}R_{eq}^3}} \qquad f_{2,2} = \frac{1}{2\pi} \sqrt{\frac{8\sigma_w}{\rho_w \epsilon R_{eq}^3}}. \quad (2)$$

Equations (2) applied to bubbles having size D_{P_2} provide: $f_{D_{P_2}}(2,0) = 12$ Hz and $f_{D_{P_2}}(2,2) = 7.4$ Hz, while for D_{P_3}: $f_{D_{P_3}}(2,0) = 9.8$ Hz and $f_{D_{P_3}}(2,2) = 6.1$ Hz. Given the complexity of the described bubbles configuration and considering the influence of the shedding mode, there is a good agreement between expected and measured frequencies.

4.3. Application to a plunging jet

The procedure described so far is now applied to the study of a plunging jet and in particular to the evolution of the air bubbles close to the free surface. The vertical water plunging jet comes out of a pipe of diameter D_J. The experimental campaign takes
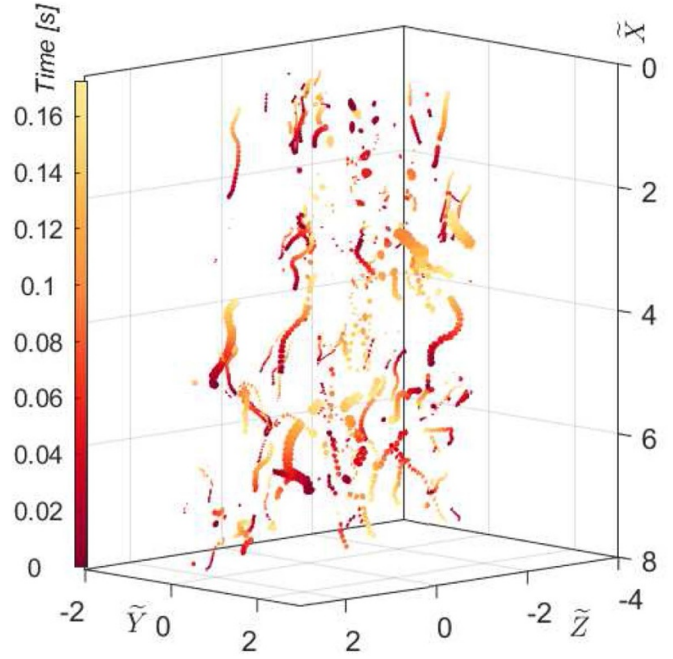

Figure 17. An overall sketch of the bubbles trajectory evolution in a plunging jet, for time $t = 0$ to $t = 2$ s. Time instants are identified by the colormap, the darker is the older. Free surface at $\widetilde{X} = 0$.

into account three sets of experiments, performed with a water flow rate equal to $Q_J = [0.5 \text{ l/s}, 0.6 \text{ l/s}, 0.7 \text{ l/s}]$, corresponding to values of the Weber number $We^{0.5}$ between 24.47 and 34.26 and of the Reynolds number Re between 3.40×10^4 and 4.76×10^4, defined as $We^{0.5} = \sqrt{(\rho_w V_J^2 D_j)/\sigma_w}$ and $\text{Re} = (\rho_w V_J D_j)/\mu_w$, where V_J is the water velocity inside the pipe with diameter D_J. These values are just below those suggested in the literature to avoid scale effects ($We^{0.5} \geq 32$ and $\text{Re} \geq 10^5$ [40]). However, this is not a constraint for this research, as the goal is to show the effectiveness of the proposed technique as a tool for the detailed analysis of air bubbles in two-phase air–water flows, also in presence of relevant void fractions.

The jet falling height H_f is equal to $5D_J$. The water flow rate has been linearly increased, starting from the minimum flow rate for the air bubble entrainment inception (Q_{J_1}), and identifying three different operating conditions.

A preliminary analysis of convergence established the total number of acquired frames required to gain robust statistics to be equal to 2000, with a frame rate equal to 130 Hz. This frame rate is settled in order to maximize the size of the acquired image and of the corresponding volume. Compared with the setup of the isolated bubble rising, it is more than halved because the image dimension is changed from 1400×300 pixels (individual rising bubble) to 1400×751 pixels. The reduced acquisition frequency limits the analysis in frequency space of the evolution of the geometric characteristics of the bubble, i.e. volume and eccentricity.

An image acquired by $Cam0$, with a snapshot of the investigated field, is reported in figure 16 together with the superimposition of 26 raw images from $fr = 0$ to $fr = 25$ for three
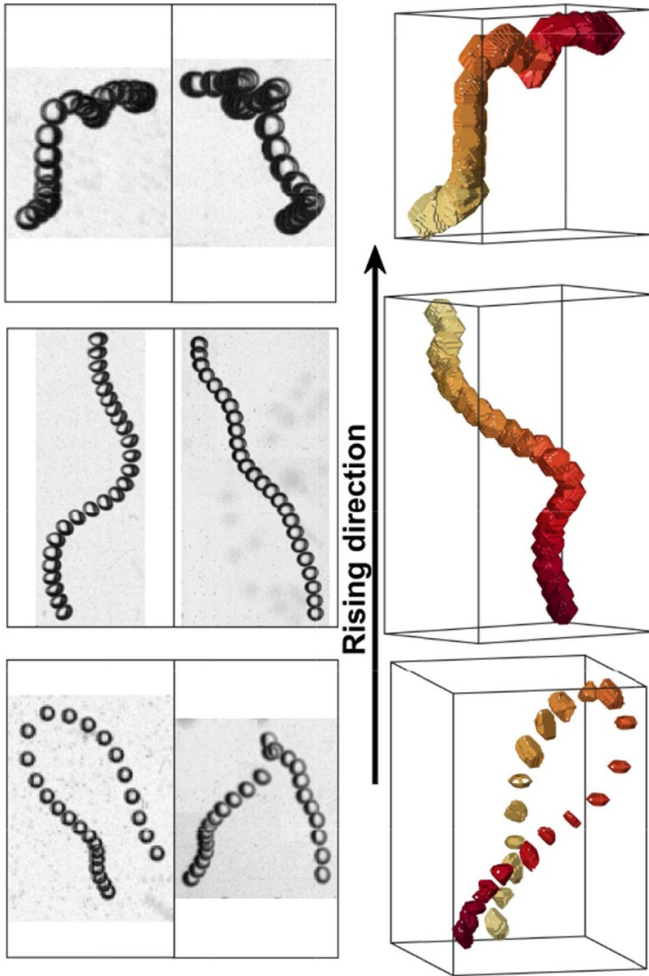
Figure 18. Examples of trajectories (red numbered *1, 2, 3* in figure 16) extracted from figure 17. Leftmost: Details of the raw data from *Cam₀* (left) and *Cam₂* (right). Rightmost: Reconstructed bubble volumes in time.

trajectories (1, 2, 3). Here the bubbles' trajectory evolution is pointed by a red arrow, while their position at snapshot acquisition time is coloured in red. The space subdivision induced by the plunging jet is overlapped for the sake of readability. The Lagrangian trajectories in figure 17 report the reconstructed sequence of positions occupied by the air bubbles from $t = 0$ to 0.2 s (26 frames). Details of bubbles' trajectories *1, 2, 3* (figure 16) are reported in figure 18: original images from two different cameras (left) and reconstructed ones (right). Air bubble trajectories in figure 17 and 18 are colored as a function of the time, moving from dark red at $t = 0$ s to bright yellow at $t = 0.2$ s. A larger number of air bubbles trajectories is observed below the jet zone in figure 16. Lateral recirculation zones are instead characterized by a lower number of air bubbles, most of them having an upward helical path similar to that observed in the rising of individual air bubbles. This is due to the lower velocity and therefore lower Weber number.

The spatial distribution of the air concentration is shown in figures 19 and 20. The air concentration is computed as the mean value inside the investigated volume (figure 1(b)) and expressed as the normalized void fraction $\widetilde{\phi}_b$, equal to 3.25%
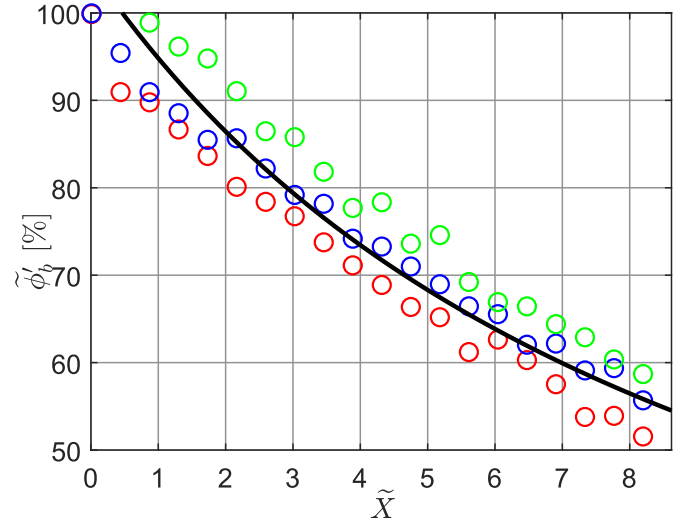

Figure 19. Axial air concentration distribution at the plane $\widetilde{Z} = 0$ and versus depth $\widetilde{X}$. Black curve indicates the decrease of the axial air concentration with the depth, following a power-law trend (equation (4)). Circles indicate: Q_{J1} (○), Q_{J2} (○), Q_{J3} (○).

for Q_{J_1}, 5.10% for Q_{J_2} and 14.86% for Q_{J_3}. The void fraction is calculated as

$$\widetilde{\phi}_b = N_b/N_f \times V_b/V_v \tag{3}$$

where N_b is the number of detected bubbles, N_f is the number of recorded frames, V_b is the mean volume of the air bubble equivalent sphere inside the voxel with volume V_v. Figure 19 reports the dimensionless axial air concentration distribution as a function of its maximum value $\phi_{b,\max}$, versus the dimensionless vertical distance from the free-surface $\widetilde{X}$. Results are well fitted by

$$\widetilde{\phi}'_b = k_0 \times \sqrt{D_j/(H_f - x')} \tag{4}$$

where k_0 is a scale coefficient, equal to 2.7 for this experimental investigation, and x' is the generic point along the streamwise direction $\widetilde{X}$. The bubbles captured by the plunging jet move vertically from the impingement point to the bottom of the tank. As the depth from the free surface increases, the bubbles tend to rise owing to the buoyancy force, which counteracts the drag force of the spreading jet on the bubbles. The axial air concentration decreases as the vertical distance from the impinging point increases, with values close to the 60% at a vertical distance of $\widetilde{X} = 7$, and shows a substantial independence upon the water flow rate. The cross-sectional air concentration distribution along the transversal direction at $\widetilde{Z} = 0$ and for different depths X, exhibits a Gaussian trend (figure 20), with a greater air concentration along the centerline of the jet zone which decreases toward the lateral recirculation zones. The Gaussian fitting is expressed as

$$\widetilde{\psi}_b = 1/(\sqrt{\pi\sigma(\widetilde{\phi})})e^{-0.5((\widetilde{Y}-\langle\widetilde{\phi}\rangle)/\sigma(\widetilde{\phi})} \tag{5}$$
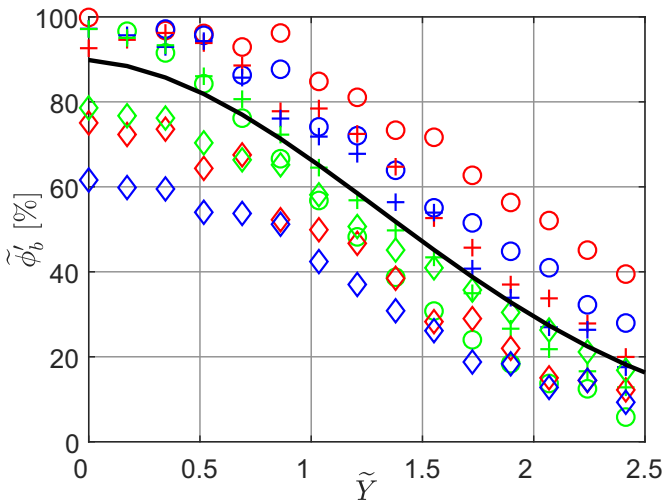
Figure 20. Cross-sectional air concentration distribution in the plane $\widetilde{Z} = 0$ vs. $\widetilde{Y}$. Curve reports a Gaussian decrease of the air concentration with the depth (equation (5)). $\bigcirc$, $+$ and $\Diamond$ markers refer to $\widetilde{X} = 2$, 4 and 6 respectively. Red, blue and green colors refer to Q_{J1}, Q_{J2} and Q_{J3}.

where $\langle \widetilde{\phi} \rangle$ and $\sigma(\widetilde{\phi})$ are respectively the mean and standard deviation of $\widetilde{\psi}_b$. The power-law trend for the dimensionless air concentration and the Gaussian trend for the cross-sectional one are both in agreement with results obtained by [2]. Moreover, despite a significant increase of the void fraction as a function of the water flow rate, both the dimensionless air concentration distributions, axial and cross-sectional, follow a similar trend regardless of the water flow rate.

5. Conclusions

This paper shows the effectiveness of a 3D volumetric shadowgraphy technique in characterizing the kinematics of air bubbles in water under different conditions. Both the measurement principle and the calibration procedure have been carefully described. In addition, an analysis of the influence of the camera system geometry has been carried out, in order to evaluate the optimal spatial arrangement of the points of view, upon which the accuracy in reconstructing of the observed object depends. The implemented technique has been validated on the benchmark case of rigid and buoyant spheres of known size, rising in still water. The detection of the shape and size of an object is made possible by space carving with a subsequent refinement of the reconstructed object. Four spheres with different radii have been tested, showing a time averaged value of the ratio between estimated and true diameter along the rising direction between 0.999 to 1.011, with an eccentricity of the fitted ellipsoid between 0.932 and 0.945. Furthermore, the accuracy in reconstructing the true volume is shown to increase with the number of points of view, with a lower coefficient of variation, indicating a more accurate and stable measurement of the observed object. It is worth mentioning that the design of an optimal setup configuration should consider the presence of a point of view orthogonal to the main reference plane, here not possible because of the presence of the free surface.

Then, the shadowgraphy technique has been used for a 3D Lagrangian tracking of a set of air bubbles released individually from the bottom of the observation tank, providing the spatial-temporal evolution of the air bubbles and the velocity along their path. Results highlight marked shape variation near the outlet section, due to the bubble detachment from the pipe nozzle, with a subsequent air bubble expansion as the depth decreases. Moreover, reduced variations of shape and size are observed for the smaller air bubbles. These findings are in agreement with the physical properties of a bubble rising in still water and are confirmed by the frequency spectra of the eccentricity recorded in time. In particular, the water forces for a small bubble do not exceed the surface tension, involving an olblate spheroid shape that minimizes the air bubble surface area. For larger bubbles, the action exerted by the water on the bubble surface overcomes the surface tension, involving a distorted spheroidal cup shape with open, unsteady wake. The projection of the present results in the $Ga-Eo$ and $Eo-Re$ phase diagrams unveil the transition that occurs in air bubble shape for the selected range of diameters, moving from an oblate spheroid rising along a zig-zag path to a spherical cup with spiraling trajectory. The wake action in the former condition locks the bubble eccentricity oscillation to the wake shedding frequency f_s, while the instability associated with the latter condition allows for the excitation of two modes whose frequencies agree quite well with data from the literature.

Finally, shadowgraphy is applied to the investigation of a vertical plunging jet at different flow rates. The detection of the boundaries of the same bubble at different times has allowed us to follow the trajectories of each air bubble also in the presence of relevant void fractions. In addition, a statistical analysis has been performed, providing the spatial distribution of the air concentration. More specifically, both the axial and cross-sectional dimensionless air concentration distributions are seen to follow similar trends with very little effect on the water flow rate. Furthermore, the air bubble paths first move downward and then rise across the lateral recirculation zones. This behavior induces the observed power-law-trend decrease of the axial air concentration distribution. On the contrary, the cross-section air concentration distribution follows a Gaussian trend, with the peak in the jet zone and decreasing values toward the lateral recirculation zones.

The promising outcome of this work encourages further refinements to improve the accuracy of the methodology with further validation tests using non-spherical reference geometries, in order to expand its range of applications to flows characterized by higher void fractions, faster time scales and larger range of bubble dimensions.

'Technology and Industrial Research for Marine Mobility - TRIM', coordinated by the National Research Council of Italy, co-funded by the Ministry of Education, University and Research.

ORCID iDs

F Di Nunno ⓘ https://orcid.org/0000-0002-8411-574X
F Alves Pereira ⓘ https://orcid.org/0000-0001-9765-8439
M Miozzi ⓘ https://orcid.org/0000-0002-6733-078X

References

[1] Sene K J 1988 Air entrainment by plunging jets *Chem. Eng. Sci.* **43** 2615–23
[2] Xu W, Chen C and Wei W 2018 Experimental study on the air concentration distribution of aerated jet flows in a plunge pool *Water* **10** 1779
[3] Felder S and Chanson H 2015 Phase-detection probe measurements in high-velocity free-surface flows including a discussion of key sampling parameters *Exp. Ther. Fluid Sci.* **61** 66–78
[4] Felder S and Chanson H 2016 Air–water flow characteristics in high-velocity free-surface flows with 50% void fraction *Int. J. Multiph. Flow* **85** 186–95
[5] Wang H, Felder S and Chanson H 2014 An experimental study of turbulent two-phase flow in hydraulic jumps and application of a triple decomposition technique *Exp. Fluids* **55** 1775
[6] Hammad K J 2010 Liquid jet impingement on a free liquid surface: PIV study of the turbulent bubbly two-phase flow *Bull. Am. Soc. Mech. Eng., Fluids Eng. Division (Publication) FEDSM* **1** 2877–85
[7] Harby K, Chiva S and Muñoz-Cobo J L 2014 An experimental study on bubble entrainment and flow characteristics of vertical plunging water jets *Exp. Ther. Fluid Sci.* **57** 207–20
[8] Kendil F Z, Danciu D V, Schmidtke M, Bousbia Salah A, Lucas D, Krepper E and Mataoui A 2012 Flow field assessment under a plunging liquid jet *Prog. Nucl. Energy* **56** 100–10
[9] Di Nunno F, Alves Pereira F, De Marinis G, Di Felice F, Gargano R, Granata F and Miozzi M 2019 Two-phase PIV-LIF measurements in a submerged bubbly water jet *J. Hydraulic Eng.* **145** 04019030
[10] Lowe D G 2004 Distinctive image features from scale-invariant keypoints *Int. J. Comput. Vis.* **60** 91–110
[11] Mira-Hernández C, Weibel J A, Vlachos P P and Garimella S V 2019 Three-dimensional liquid-vapor interface reconstruction from high-speed stereo images during pool boiling *Int. J. Heat Mass Transf.* **136** 265–75
[12] Qu X, Goharzadeh A, Khezzar L and Molki A 2013 Experimental characterization of air-entrainment in a plunging jet *Exp. Thermal Fluid Sci.* **44** 51–61
[13] Bröder D and Sommerfeld M 2007 Planar shadow image velocimetry for the analysis of the hydrodynamics in bubbly flows *Meas. Sci. Technol.* **18** 2513–28
[14] Lindken R and Merzkirch W 2002 A novel PIV technique for measurements in multi-phase flows and its application to two-phase bubbly flows *Exp. Fluids* **33** 814–25
[15] Qu X L, Khezzar L, Danciu D, Labois M and Lakehal D 2011 Characterization of plunging liquid jets: A combined experimental and numerical investigation *Int. J. Multiph. Flow* **37** 722–31
[16] Settles G 2001 Schlieren and Shadowgraph Techniques: Visualizing Phenomena in Transparent *Media Engineering online library* (Heidelberg: Springer)
[17] Fu Y and Liu Y 2016 Development of a robust image processing technique for bubbly flow measurement in a narrow rectangular channel *Int. J. Multiph. Flow* **84** 217–28
[18] Karn A, Ellis C, Arndt R and Hong J 2015 An integrative image measurement technique for dense bubbly flows with a wide size distribution *Chem. Eng. Sci.* **122** 240–9
[19] Lau Y M, Deen N G and Kuipers J A M 2013 Development of an image measurement technique for size distribution in dense bubbly flows *Chem. Eng. Sci.* **94** 20–9
[20] Tomiyama A, Celata G P, Hosokawa S and Yoshida S 2002 Terminal velocity of single bubbles in surface tension force dominant regime *Int. J. Multiph. Flow* **28** 1497–1519
[21] Hosoda S, Abe S, Hosokawa S and Tomiyama A 2014 Mass transfer from a bubble in a vertical pipe *Int. J. Heat Mass Transfer* **69** 215–22
[22] Fu Y and Liu Y 2018 3d bubble reconstruction using multiple cameras and space carving method *Meas. Sci. Technol.* **29** 075206
[23] Pereira F, Avellan F and Dupont P 1998 Prediction of cavitation erosion: An energy approach *J. Fluids Eng.* **120** 719–27
[24] Lucas B D and Kanade T 1981 An iterative image registration technique with an application to stereo vision *Proc. 7th Int. Conf. on Artificial Intelligence IJCAI'81* pp 674–9
[25] Tsai R Y 1986 An efficient and accurate camera calibration technique for 3d machine vision *Proc. IEEE Comput. Soc. Conf. Comput. Vis. Pattern Recognit.* 364–74 XP001004843
[26] Li Q and Griffiths J G 2004 Least squares ellipsoid specific fitting *Proc.- Geometric Modeling and Processing 2004* pp 335–40
[27] Bouguet J Y 2008 A release of a camera calibration toolbox for matlab (http://www.vision.caltech.edu/bouguetj/calib_doc/)
[28] Heikkila J and Silven O 1997 Four-step camera calibration procedure with implicit image correction *Proc. IEEE Computer Conf. on Computer Vision and Pattern Recognition* 1106–12
[29] Zhang Z 2000 A flexible new technique for camera calibration *IEEE Trans. Pattern Anal. Mach. Intell.* **22** 1330–4
[30] Dai J S 2015 Euler–Rodrigues formula variations, quaternion conjugation and intrinsic connections *Mech. Mach. Theory* **92** 144–52
[31] van de Hulst H C 1957 *Light Scattering From Small Particles* (New York: Wiley)
[32] Ridler T W and Calvard S 1978 Picture thresholding using an iterative selection method *IEEE Trans. Syst. Man Cybern.* **SMC-8** 630–2
[33] Vincent L, P S 1991 Watersheds in digital spaces: an efficient algorithm based on immersion simulations *IEEE Trans. Pattern Anal. Mach. Intell.* **13** 583–98
[34] Miozzi M, Corvaro S, Alves Pereira F and Brocchini M 2019 Wave-induced morphodynamics and sediment transport around a slender vertical cylinder *Adv. Water Resour.* **129** 263–80
[35] Pereira F, Stüer H, Graft E C and Gharib M 2006 Two-frame 3d particle tracking *Meas. Sci. Technol.* **17** 1680–92
[36] Sharaf D M, Premlata A R, Tripathi M K, Karri B and Sahu K C 2017 Shapes and paths of an air bubble rising in quiescent liquids *Phys. Fluids* **29** 122104
[37] Bhaga D and Weber M E 1981 Bubbles in viscous liquids: shapes, wakes and velocities *J. Fluid Mech.* **105** 61–85
[38] Zhang J and Ni M 2017 What happens to the vortex structures when the rising bubble transits from zigzag to spiral? *J. Fluid Mech.* **828** 353–73
[39] Lunde K and Perkins R J 1998 Shape oscillations of rising bubbles *Appl. Sci. Res. (The Hague)* **58** 387–408
[40] Pfister M and Chanson H 2014 Two-phase air–water flows: Scale effects in physical modeling *J. Hydrodynamics* **26** 291–8